Laser processing over a large area by wavefront-controlled scanning

Xinpeng Du, Arifur Rahaman, Aravinda Kar, Michael Chase, Dave Wolfe, John Mathy, and Xiaoming Yu

View Online   Export Citation   CrossMark

ARTICLES YOU MAY BE INTERESTED IN

READ NOW!
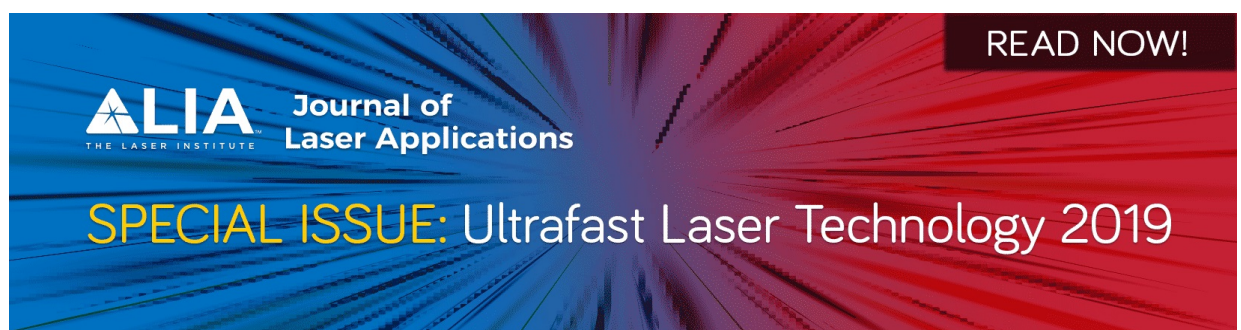
ALIA Journal of Laser Applications

SPECIAL ISSUE: Ultrafast Laser Technology 2019

Laser processing over a large area by wavefront-controlled scanning

Xinpeng Du,[1] (iD) Arifur Rahaman,[1] (iD) Aravinda Kar,[1] (iD) Michael Chase,[2] Dave Wolfe,[2] (iD) John Mathy,[2] and Xiaoming Yu[1,a)]

AFFILIATIONS

[1]The College of Optics and Photonics (CREOL), University of Central Florida, 4304 Scorpius Street, Orlando, Florida 32816
[2]Elsner Engineering Works, Inc., 475 Fame Avenue, Hanover, Pennsylvania 17331

[a)]Author to whom correspondence should be addressed; electronic mail: yux@creol.ucf.edu

ABSTRACT

In the processing of laser materials, the scanning area is limited by the extent to which the laser focus can be maintained within a plane. In order to increase the processing area, one has to enlarge the size of the laser focal spot, and, therefore, reduce the peak intensity and spatial resolution. In this paper, the authors report on a method that extends the processing area by controlling the wavefront of a laser beam using adaptive optics. By adding Zernike modes to the laser beam wavefront, the axial (along the beam propagation direction) location of the focal spot can be tuned within a range larger than the confocal length (two times the Rayleigh length), while the lateral spot size (and, thus, peak intensity and resolution) is maintained throughout the tuning range. A wave propagation model that simulates the propagation of a wavefront-controlled beam is used to compare with the experimental results, which are also confirmed by Zemax calculation. Laser trepanning of circular holes with consistent size on a wide polypropylene sheet is demonstrated. This work shows the potential of tailoring the phase of a laser beam for improving the accuracy and throughput in large-area laser processing of materials.

INTRODUCTION

Ultrafast laser has been widely researched for high-precision and high-robustness processing on materials such as metals,[1–4] ceramics,[5–8] glasses,[9] and polymers.[10–15] Many functional structures and devices are, thus, fabricated due to their excellent processing properties of little to no heat affected zone, clean processing quality, good repeatability, and no requirement of postprocessing.[16–18]

Regardless of applications, there are two major types of setups for laser processing. The first type is to utilize a laser head above the workpiece with the height fixed at the focal length of the converging lens in the laser head, and the workpiece can be mounted on a translation stage to control focusing and scanning trajectory. However, this configuration can be slow in scanning, which is limited by the mechanical motion mechanism. The second type is to utilize an f-theta lens and a galvo-scanner/polygon scanner to deliver the laser beam to the workpiece with a flat focal plane.[19,20] But this configuration often has a limited field of view determined by the f-theta lens. To date, it has remained challenging to obtain fast scanning speed with a large field of view.

Recently, adaptive optics has been widely developed to dynamically correct the aberration in the wavefront. The wavefront is a 2D map of the phase on a plane normal to the wave propagation direction. To the first order, wavefront aberration is due to the difference of the optical path length (OPL) among different ray tracing paths. Similarly, by introducing OPL change, the wavefront can also be modified for compensating the aberration.

Deformable mirrors (DMs) are one type of adaptive optics devices that can be used to change the wavefront.[21,22] A DM consists of many mirror segments that can be controlled independently to shift and/or tilt. As any wavefront can be decomposed into Zernike modes[23] and low-order Zernike modes can be achieved by setting each segment mirror at the right shift and tilt angle, any wavefront can be obtained by the superposition of all segment mirrors, thus compensating wavefront distortion.

Another type of adaptive optics is the liquid-crystal spatial light modulator. It can modify the intensity, phase, or polarization of a laser beam by applying a signal to liquid-crystal pixels to change properties such as refractive index. It has been used in material processing as well.[24–27]

In this paper, the ability of an adaptive optics is demonstrated for large-area scanning by maintaining the focal plane on a workpiece. With a galvo-scanner placed at 1074 mm above a workpiece and the adaptive optics to change the wavefront, this study shows that a scanning width of 846 mm can be achieved. Over this width, the beam radius is maintained to be $86.4 \pm 7.3\,\mu$m. With the constant beam radius, a trepanning drilling method was applied on a polypropylene sheet with a thickness of $250\,\mu$m and the hole size was maintained to be $242.2 \pm 9.0\,\mu$m. In addition, a wavefront model is built to calculate the focal plane position which is verified by the experimental data. Zemax modeling was also developed to optimize the Zernike coefficient so that the laser beam can be focused at a given image plane position.

EXPERIMENT

The experimental setup is schematically illustrated in Fig. 1. A femtosecond laser (Pharos, Light Conversion) was applied to emit a Gaussian beam with a central wavelength of 1027 ± 5 nm, $1/e^2$ spot radius 2.1 mm, pulse duration 170 fs, repetition frequency 1 kHz, and average power 1 W into the system. A focusing system consisting of three lenses, L_1 (LC1120-B, focal length $f = -100$ mm, Thorlabs), L_2 (LA1908-B, $f = 500$ mm, Thorlabs), and L_3 (LA1464-B, $f = 1000$ mm, Thorlabs), was used to initially focus the laser beam to a reference position on the workpiece surface. The negative lens L_1 was mounted on a linear stage (423 Series, Newport) motorized by an actuator (CMA-25CCCL, Newport) to allow fine tuning.

A deformable mirror (PTT111, Iris AO, 37 mirror segments, 3.5 mm in aperture diameter) was inserted into the optical system to adjust the wavefront to change the focal length. An x-y galvo-scanner (hurrySCAN®20, SCANLAB) was used to deliver the beam to the workpiece surface and do the scanning. The scanner was placed at a height of 1074 mm above the working plane to cover a distance of 846 mm on the workpiece surface within a 43° field of view. The synchronization between laser on/off and scanning position was controlled by the TTL signal from the scanner to the external control connection of the laser. The synchronization of the DM to the scanner was achieved through the wait set/release of the DM. The operation was performed with a LABVIEW program.

Nine positions with equal spacing over the entire width of the workpiece (F_1 and F_2 are the same positions as shown in Fig. 1) are shown in Fig. 2, where the images of the spots without and with using the DM are illustrated in row A and row B, respectively. The spots were imaged with a CMOS camera (SME-B050-U, Mightex).

To maintain the focus at each position, a detection card was placed at the nine positions on the workpiece. The laser power delivered to the workpiece was set to the critical power (80 mW) that could just generate plasma on the detection card when the laser spot was in focus. By manually changing the DM setting, focus was obtained and the spot was measured at each position. The settings were recorded and could be controlled by computerized automation for manufacturing applications.

A polypropylene sheet (Phaser® 740, Tektronix, Part No. 016-1654-00, $250\,\mu$m in thickness) was used as the workpiece in the trepanning experiment using DM-corrected laser spots. The trepanning radius was $195\,\mu$m and the laser power on the
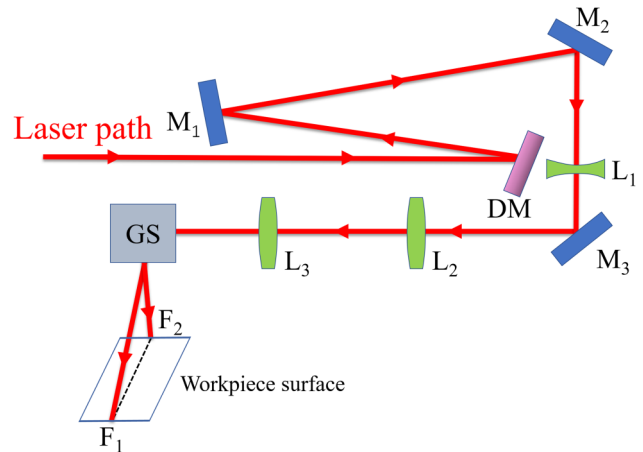

FIG. 1. Schematic diagram of the experimental setup and the laser path. DM, deformable mirror; M, optical mirror; L, lens. GS, galvo-scanner. The GS delivers the laser beam to do the scanning along the line F_1F_2 on the workpiece surface.

workpiece was 250 mW at the laser repetition frequency of 1 kHz. The exposure time to machine each hole was about 4 s. The SEM images of the resulting holes are presented in row C of Fig. 2. The taper angles of each hole on the left and right walls were measured with a 2D profilometer, and the resulting depth profiles are
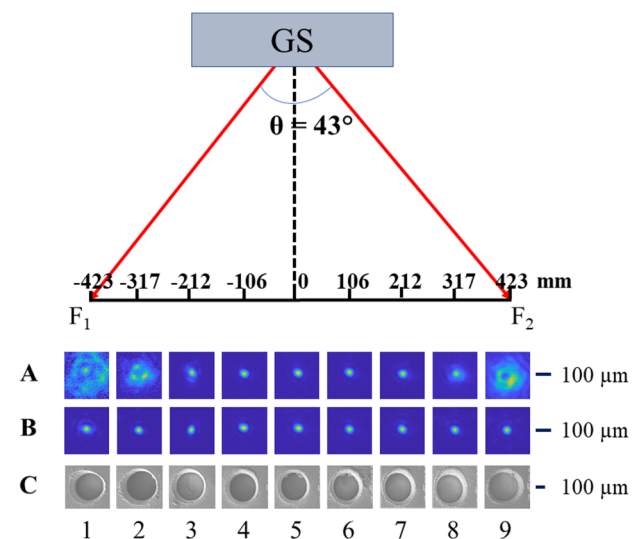
FIG. 2. Images of laser focal spots and laser-trepanned holes at nine different positions along F_1F_2 (see Fig. 1). Rows A and B are the laser spots without DM (no wavefront modulation) and with DM (wavefront modulation to correct the defocus of row A), respectively. The spot radius ($1/e^2$) is calculated to be $86.4 \pm 7.3\,\mu$m in row B. Row C shows the SEM images of the drilled holes by using the corresponding laser spots in row B.
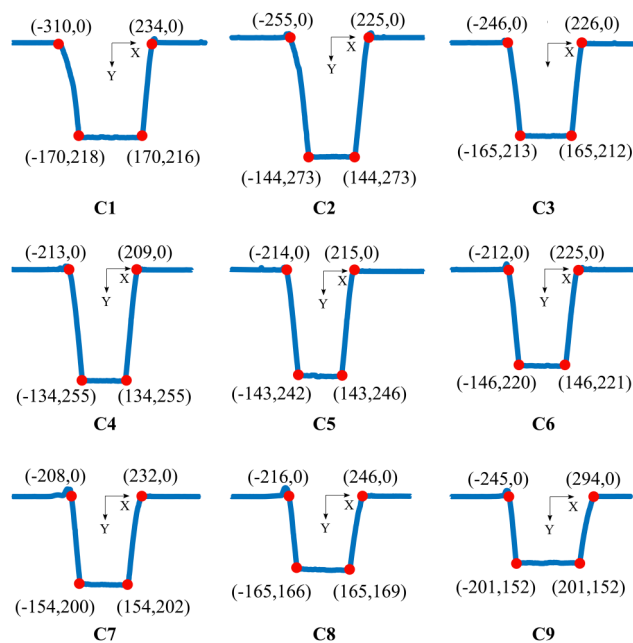
FIG. 3. Depth profiles of the holes measured with a 2D profilometer. Each profile is a compilation of the downhill scans for the profilometer probe traversing from the left to right and right to left directions for the left and right sidewalls of the holes, respectively. The numbers in the parentheses are the (x, y) coordinates in the unit of micrometer. The hole depth profiles C1–C9 correspond to the holes labeled 1–9 in row C of Fig. 2.

presented in Fig. 3. The diameters of the holes at the top surface of the sample varied in the range of 422–544 μm. The machined depth across the field of view was 216 ± 37 μm. So, the average ablated depth per pulse was 0.054 ± 0.009 μm.

Due to the geometry of the profilometer stylus, the scans in the downhill and uphill directions were found to yield different taper angles. The downhill scan was determined to be more accurate by running the stylus over a standard sample containing a perfect vertical wall, that is, a 0° taper angle. The downhill scans across each hole were, therefore, utilized to construct the complete profile of the hole depth, as displayed in Fig. 3. However, the geometrical size of the stylus affected the resolution in measuring the taper angle. Even in the downhill scanning direction, the stylus was unable to produce the 0° taper angle of the standard sample, and instead registered a taper angle of 15 ± 1°. So, the measured taper angles can be corrected by subtracting 15° from the measured data to account for the effect of the stylus size. The taper angles of each hole on the left and right sidewalls were measured, and both the measured and the corrected angles are listed in Table I.

RESULTS AND DISCUSSION

Processing parameters

At 250 mW and 1 kHz with a spot radius 86.4 μm, the peak laser fluence is estimated to be 2.2 J/cm². With pulse duration

TABLE I. Taper angles in the unit of degree for each hole on the left and right side-walls. The hole identification numbers (ID) C1–C9 correspond to the holes labeled 1–9 in row C of Fig. 2.

Hole ID	Measured taper[a]		Corrected taper[b]	
	Left wall	Right wall	Left wall	Right wall
C1	33	16	18	1
C2	22	17	7	2
C3	21	16	6	1
C4	17	16	2	1
C5	17	17	2	2
C6	17	20	2	5
C7	15	21	0	6
C8	17	26	2	11
C9	16	31	1	16

[a]Taper angles as measured before correction for the stylus size.
[b]Taper angles after correction for the stylus size.

170 fs, the estimated peak intensity is 1.3×10^{13} W/cm². As the machine depth of the PP sheet is around 216 μm, and the linear absorption coefficient for PP at 1030 nm is about 50 cm^{-1},[12] the intensity remains almost constant in the film. Therefore, the holes drilled in the PP film are due to nonlinear absorption. Given that PP has a bandgap of 7 eV,[28] it is estimated that six photons are needed to initiate electronic excitation.

Wavefront control

The spot sizes are significantly affected by tuning the wavefront, as seen from Fig. 2. Without using the DM, the beam can remain focused only within its confocal range (estimated to be 45 mm), which can lead to a drilling range of 424 mm, as seen from A3 to A7 in row A of Fig. 2. Beyond this range, the spot is out of focus as the optical path length to the edge is different from the length to the center. By using the DM to control the wavefront at each position, the spot sizes are almost constant over the entire width of the workpiece (row B in Fig. 2). These constant laser parameters will enable consistent processing of materials in practice.

The amount of change of the wavefront by using the DM can be explained in Fig. 4. Initially, the DM takes the shape of a flat surface as the reference plane. When the Zernike modes are set to change the phase, the surface becomes nonplanar. As the entire optical system in our case is axisymmetric, only the defocus mode (modal 4) of the Zernike series is considered. It is found that the next axisymmetric Zernike mode, which is the third order spherical mode (modal 11), has negligible contribution to make to the observed beam profile, so it is not used in this study. The polynomial expression of Zernike modal 4 Z_4 in the cylindrical coordinate system is

$$Z_4 = \sqrt{3}\,(2\rho^2 - 1). \tag{1}$$

Here, ρ is the radial distance normalized to the aperture.

The curved surface profile AOD of the DM is a paraboloid expressed by the Zernike modal 4 scaled by a coefficient A_4. In the
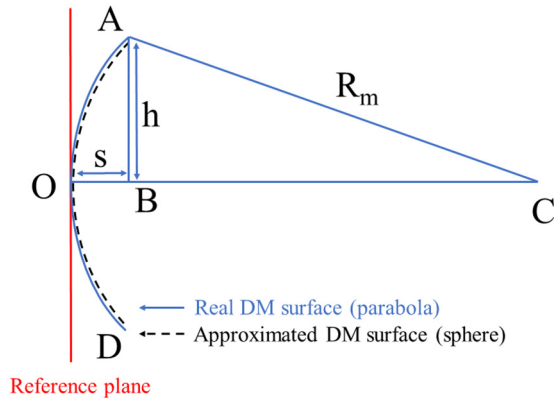
FIG. 4. Schematic diagram showing the curvature change of the deformable mirror as a function of the sag distance s (*OB*) which is determined by the modal 4 Zernike coefficient. In calculation, the DM curvature *AOD* (solid blue line) is approximated by a spherical curvature *AOD* (dashed black line). The radius of the curvature of the sphere is R_m centered at Point *C*. The height of the edge point to the optical axis (*OC*) is *h*.

calculation, the paraboloid curvature is approximated by the curvature of a spherical surface passing the points *A*, *O*, and *D*. Assuming that the center of the sphere is at *C*, the radius of the curvature of the sphere will be R_m (length of *AC*). The entrance diameter of the DM is 3.5 mm ($h = 1.75$ mm in Fig. 4). For the sag distance s (*OB*), it is equivalent to the length difference between $\rho = 0$ and $\rho = 1$,

$$A_4 Z_4 = \sqrt{3} A_4 (2\rho^2 - 1) \Rightarrow s = 2\sqrt{3} A_4 . \tag{2}$$

Then, the radius R_m can be calculated in the right triangle *ABC* as

$$R_m^2 = (R_m - s)^2 + h^2 \Rightarrow R_m = \frac{h^2 + s^2}{2s} \approx \frac{h^2}{2s} = \frac{h^2}{4\sqrt{3} A_4} . \tag{3}$$

Here, the square of the sag distance is ignored as it is very small compared with the square of *h*.

The incident wavefront radius of curvature at the entrance of the DM has been calculated to be $R_i = 19$ m. Assuming that the angle between the laser propagation direction and the normal of the DM is small, the resultant wavefront radius R_o of curvature after the DM can be calculated[29] as

$$\frac{1}{R_i} = \frac{1}{R_o} + \frac{2}{R_m} . \tag{4}$$

As a result, the curvature of the resultant wavefront can be controlled by setting the modal 4 coefficient A_4. Thus, the image plane position can be adjusted by setting A_4.

In order to verify the calculation, three positive lenses with different focal lengths placed at 170 mm after the DM were applied to measure the position of the image plane by Eqs. (5)–(7)[30] as

follows:

$$z' = f + \frac{f^2(z - f)}{(z - f)^2 + (z_0)^2}, \tag{5}$$

$$R = z \left[1 + \left(\frac{z_0}{z} \right)^2 \right], \tag{6}$$

$$z_0 = \frac{\pi w^2}{\lambda} , \tag{7}$$

where *z* is the distance from the object, *z'* is the distance from the image, z_0 is the Rayleigh range, *f* is the focal length of each lens used successively, *R* is the radius of the wavefront curvature, *w* is the $1/e^2$ spot size, and *λ* is the wavelength. When the position of interest is far beyond the laser waist position ($z \gg z_0$), the radius of the wavefront curvature can be approximated to be the distance to the waist position ($R \approx z$).

The calculation and the measurement results of the image plane positions are shown in Fig. 5.

For a short focal length ($f = 150$ mm), the image plane position is approximately linear with the modal 4 coefficient, which is well supported by experiment.

As the focal length gets longer, the deviation between calculation and experiment gets increased. This is perhaps due to the fact that a longer focal length results in a larger confocal range which adversely affects the judgment of the image plane position. Another reason could be the approximation of the DM curvature by a spherical curvature. The approximation of the small angle by using Eq. (4) could also result in some error. But generally, both calculation and experiment show similar trends.
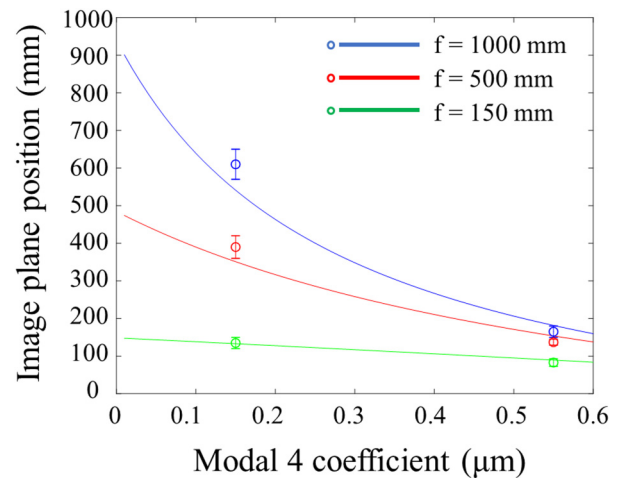

FIG. 5. The image plane position (referred to the location of the lens) as a function of the modal 4 coefficient with three different positive lenses. The solid lines represent the calculation results. The circles represent the experimental measurements.

Zemax modeling

Setting the modal 4 coefficient A_4 to change the image plane position is the "forward method" of modeling the optical system. The "backward method" is to set the image plane position and determine A_4 to get focus on the image plane. The latter is beneficial because the working distance of a setup can be set or known in advance.

For our optical setup of multiple optic elements, Zemax was applied to do the modeling. The configuration shown in Fig. 1 was imported into Zemax. The DM was simulated by a surface with a surface type called "Zernike Standard Phase." Initially, Zemax was used in the forward modeling. The wavefront directly modified by the DM was simulated by Zemax and compared with the real segment mirror placement, as shown in Fig. 6.
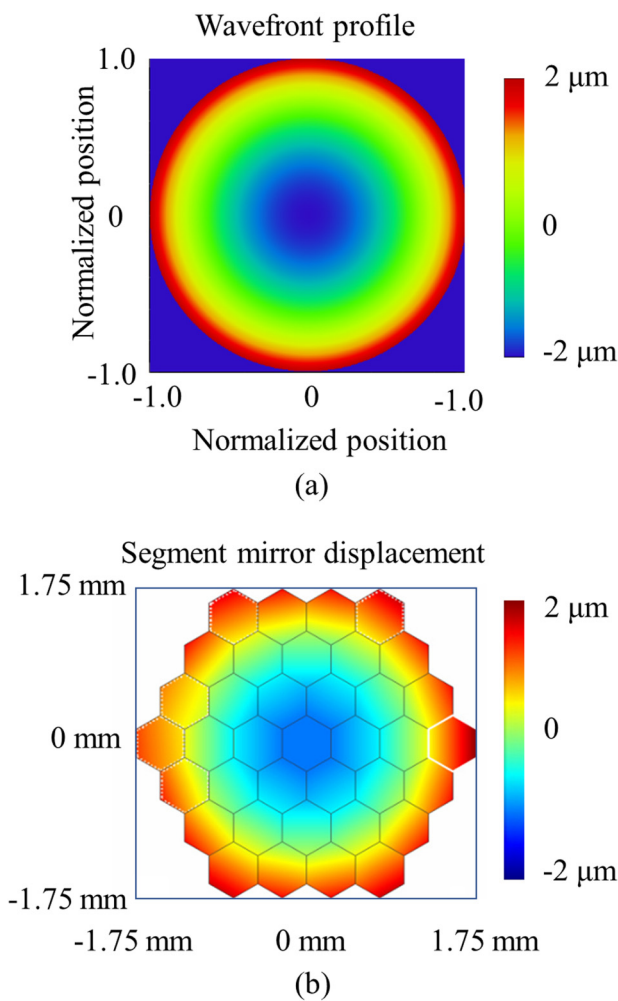

(a)

(b)

FIG. 6. (a) Wavefront profile (converted to displacement) induced by the Zernike modal 4 with the coefficient 0.6 μm from Zemax simulation. (b) Displacement of each segment mirror of the deformable mirror by setting the same modal 4 coefficient obtained from the user interface of the software.

Figure 6(a) shows the wavefront profile with the modal 4 coefficient equal to 0.6 μm with normalized position on the reference plane, simulated by Zemax. Figure 6(b) shows the displacement of the real segment mirrors at the same modal 4 coefficient, obtained from the user interface of the DM software. Both show similar characteristics, indicating that the forward simulation is accurate. The selection of $A_4 = 0.6$ μm is to consider the displacement limit of the segment mirror on the edge (2 μm).

Then, the backward simulation was applied in Zemax. The back focal distance (image plane position) referred to the vertex of the last lens was gradually changed from 1300 to 1200 mm at a step size of 5 mm. The back focal distance to the edge of the workpiece is around 1300 mm. The back focal distance to the center position is around 1220 mm. At each position, the modal 4 coefficient was set to be a variable that needs to be optimized. The merit function was to make the spot size smallest at the corresponding image plane position. After optimization, the modal 4 coefficient was calculated and returned. In this way, a series of modal 4 coefficients as a function of the focal shift (the amount of the change in the back focal distance referred to the reference position) was obtained, which can be compared with the experimental results as explained in the Experimental section. Notice that the focal shift is symmetric around the center position to each side. Both the modeling and the experimental result are compared in Fig. 7.

It can be seen from Fig. 7 that Zemax predicts a linear trend between the focal shift and the modal 4 coefficient. As our three-lens system has an effective focal length of 272 mm, the linear trend matches the single-lens result, as shown in Fig. 5. The performance of the setup is closer to the behavior of a short focal length, which is within our expectation. Better matches are observed at longer focal shift positions than shorter ones. Generally, both the experiment and the Zemax modeling match each other.
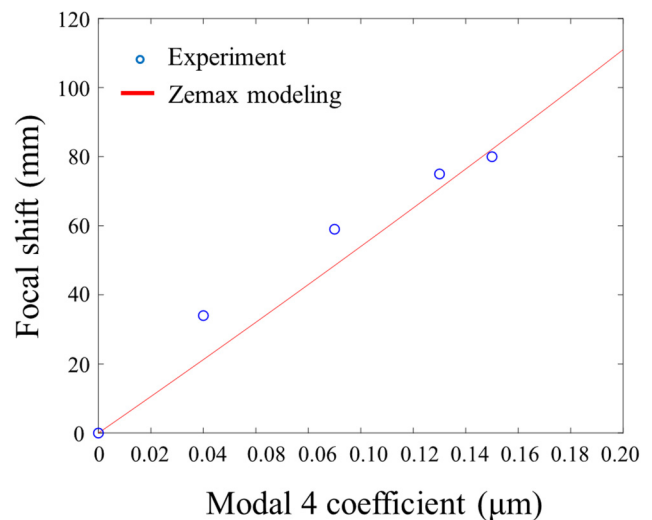

FIG. 7. Modal 4 coefficient as a function of the total focal shift of the optic system. The solid line represents the calculation results from Zemax. The circles represent the experimental data.

CONCLUSION

This paper illustrates a new method for increasing the range of laser scanning using adaptive optics. The wavefront of the laser beam is controlled using a DM to adjust the focal position, which yields a consistent spot size across the scanning field. Both forward and backward Zemax modeling were used to support the experimental results and analysis. A method of modulating the curvature of the DM mirror is presented to achieve the same focal spot size on the workpiece surface along the laser scanning direction. This technique can be adopted for other processing modalities such as cutting, drilling, marking, and thin film deposition, by inserting an adaptive optical device into the existing beamline.

ACKNOWLEDGMENTS

REFERENCES

[1]Q. Wang, S. Luo, Z. Chen, H. Qi, J. Deng, and Z. Hu, "Drilling of aluminum and copper films with femtosecond double-pulse laser," Opt. Laser Technol. **80**, 116–124 (2016).

[2]A. Gruner, J. Schille, and U. Loeschner, "Experimental study on micro hole drilling using ultrashort pulse laser radiation," Phys. Procedia **83**, 157–166 (2016).

[3]G. Casalino, A. M. Losacco, A. Arnesano, F. Facchini, M. Pierangeli, and C. Bonserio, "Statistical analysis and modelling of an Yb: KGW femtosecond laser micro-drilling process," Proc. CIRP **62**, 275–280 (2017).

[4]D. Haasler and J. Finger, "Investigation of heat accumulation effects during deep hole percussion drilling by high power ultrashort pulsed laser radiation," J. Laser Appl. **31**, 022201 (2019).

[5]K. Mishchik, K. Gaudfrin, and J. Lopez, "Drilling of through holes in sapphire using femto-second laser pulses," J. Laser Micro Nanoeng. **12**, 321–324 (2017).

[6]Y. Liu, R. Zhang, W. Li, J. Wang, X. Yang, L. Cheng, and L. Zhang, "Effect of machining parameter on femtosecond laser drilling processing on SiC/SiC composites," Int. J. Adv. Manuf. Technol. **96**, 1795–1811 (2018).

[7]D. Deng, Y. Xie, L. Chen, and X. Chen, "Experimental investigation on laser micromilling of SiC microchannels," Int. J. Adv. Manuf. Technol. **101**, 9–21 (2019).

[8]H. Shin and W. Jeong, "Femtosecond laser micromachining of zirconia green bodies," Int. J. Addit. Subtractive Mater. Manuf. **1**, 104–117 (2017).

[9]Y. Ito, R. Yoshizaki, N. Miyamoto, and N. Sugita, "Ultrafast and precision drilling of glass by selective absorption of fiber-laser pulse into femtosecond-laser-induced filament," Appl. Phys. Lett. **113**, 061101 (2018).

[10]B. Wang, X. C. Wang, H. Y. Zheng, and Y. C. Lam, "Thermal effect of femtosecond laser polystyrene processing," Opt. Laser Technol. **117**, 244–250 (2019).

[11]A. Rahaman, A. Kar, and X. Yu, "Thermal effects of ultrafast laser interaction with polypropylene," Opt. Express **27**, 5764 (2019).

[12]A. Rahaman, A. Kar, and X. Yu, "Time-resolved measurements of optical properties in ultrafast laser interaction with polypropylene," Opt. Express **28**, 2640–2648 (2020).

[13]J. Krüger and W. Kautek, "Femtosecond-pulse visible laser processing of transparent materials," Appl. Surf. Sci. **96–98**, 430–438 (1996).

[14]S. Baudach, J. Bonse, J. Krüger, and W. Kautek, "Ultrashort pulse laser ablation of polycarbonate and polymethylmethacrylate," Appl. Surf. Sci. **154**, 555–560 (2000).

[15]S. Baudach, J. Bonse, and W. Kautek, "Ablation experiments on polyimide with femtosecond laser pulses," Appl. Phys. A: Mater. Sci. Process. **69**, 395–398 (1999).

[16]M. Terakawa, "Femtosecond laser processing of biodegradable polymers," Appl. Sci. **8**, 1123 (2018).

[17]S. Hypsh and G. Shannon, "Femtosecond laser processing of metal and plastics in the medical device industry precision machining with no thermal effects and minimal post processing," Amada Miyachi America **1**, 1–6 (2014).

[18]T. N. Kim, K. Campbell, A. Groisman, D. Kleinfeld, and C. B. Schaffer, "Femtosecond laser-drilled capillary integrated into a microfluidic device," Appl. Phys. Lett. **86**, 201106 (2005).

[19]F. Di Niso, C. Gaudiuso, T. Sibillano, F. P. Mezzapesa, A. Ancona, and P. M. Lugarà, "Role of heat accumulation on the incubation effect in multi-shot laser ablation of stainless steel at high repetition rates," Opt. Express **22**, 12200–12210 (2014).

[20]J. Schille, L. Schneider, A. Streek, S. Kloetzer, and U. Loeschner, "High-throughput machining using high average power ultrashort pulse lasers and ultrafast polygon scanner," in *Laser-Based Micro- and Nanoprocessing, San Francisco, CA, 4 March 2016* (SPIE, Bellingham, WA, 2016), X 9736, p. 97360R.

[21]S. Li, L. Zhou, C. Cui, K. Wang, X. Yan, Y. Wang, L. Ding, Y. Wang, and Z. Lu, "Wavefront shaping by a small-aperture deformable mirror in the front stage for high-power laser systems," Appl. Sci. **7**, 1–9 (2017).

[22]F. Druon, G. Cheriaux, A. Maksimchuk, and G. Mourou, "Wave-front correction of femtosecond terawatt laser using a deformable mirrors," Conf. Lasers Electro-Optics Eur. Tech. Dig. **23**, 1043–1045 (1998).

[23]R. J. Noll, "Ernike polynomials and atmospheric turbulence," J. Opt. Soc. Am. **66**, 207–211 (1976).

[24]J. P. Parry, R. J. Beck, J. D. Shephard, and D. P. Hand, "Application of a liquid crystal spatial light modulator to laser marking," Appl. Opt. **50**, 1779–1785 (2011).

[25]Y. Di Chen, W. J. Tsai, S. H. Liu, and J. Bin Horng, "Hierarchical micro/nanostructures generated by femtosecond laser beams modified through a liquid-crystal spatial light modulator," Appl. Surf. Sci. **353**, 568–573 (2015).

[26]J. J. J. Kaakkunen, I. Vanttaja, and P. Laakso, "Fast micromachining using spatial light modulator and galvanometer scanner with infrared pulsed nanosecond fiber laser," J. Laser Micro/Nanoeng. **9**, 37–41 (2014).

[27]J. Ouyang, W. Perrie, O. J. Allegre, T. Heil, Y. Jin, E. Fearon, D. Eckford, S. P. Edwardson, and G. Dearden, "Tailored optical vector fields for ultrashort-pulse laser induced complex surface plasmon structuring," Opt. Express **23**, 12562–12572 (2015).

[28]Y. Ohki, N. Fuse, and T. Arai, "Band gap energies and localized states in several insulating polymers estimated by optical measurements," in *Annual Report—Conference on Electrical Insulation and Dielectric Phenomena, CEIDP, West Lafayette, IN, 17–20 October 2010* (IEEE, Piscataway, NJ, 2010), pp. 1–4, available at https://www.tib.eu/en/search/id/TIBKAT%3A655964193/.

[29]B. E. A. Saleh and M. C. Teich, *Fundamentals of Photonics*, 2nd ed. (John Wiley & Sons, Inc., Hoboken, NJ, 2007).

[30]F. L. Pedrotti, L. M. Pedrotti, and L. S. Pedrotti, *Introduction to Optics*, 3rd ed. (Cambridge University Press, Cambridge, UK, 2017).